Article

Combustion of Al Nanoparticles Coated with Nitrocellulose/Ethanol/Ether Molecules by Equilibrium Molecular Dynamics Simulations

Yue Chu, Lei Wang, Pingan Liu,* and Penghua Sui

Read Online

ACCESS | Metrics & More | Article Recommendations

ABSTRACT: Al nanoparticles (ANPs) have high reactivity, but they are easily inactivated by external oxidants. To improve their surface properties, we coat ANPs with a nitrocellulose (NC)/ethanol/ether solution. Comparative discussions are raised from the coating to the combustion process. Our results show that NC/ethanol/ether forms a dense coating layer on the surface of annealed ANPs and passivates ANPs through physical and chemical adsorption. The coating layer can block the contact between the active Al atoms and O_2 molecules at low temperatures. In the ignition phase, the NC/ethanol/ether coating layer can increase the density of the O_2 molecules around the ANPs and the surface temperature of ANPs. At the end of the ignition phase, the number of O atoms adsorbed on the surface of NC/ethanol/ether coating-passivated ANPs (csANPs) and NC/ethanol/ether coating-annealed ANPs (cANPs) increased by about 60 and 50%, respectively, compared with passivated ANPs (sANPs). Since the desorption and diffusion of the coating layer will expose more reaction sites, ANPs have a shorter ignition delay and a lower ignition temperature. According to the change in atomic displacement, the combustion stage can be divided into three stages: surface oxidation/core melting diffusion, combustion inward propagation, and uniform combustion. The decomposition of NC molecules can increase the combustion speed, combustion time, and efficiency of ANPs. Such improvement will enable ANPs to obtain better storage and combustion performance and play a stronger role in the field of energetic materials.
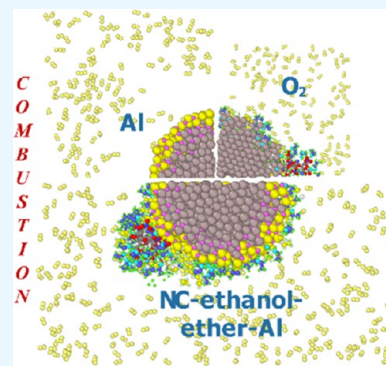
1. INTRODUCTION

An energetic material is a kind of compound or mixture containing explosive groups or combustibles and oxidants. Under certain external stimuli, it can conduct redox reactions alone and release a large amount of energy (usually accompanied by a large amount of gas and heat). As typical energetic materials, Al nanoparticles (ANPs) play an important role in propellants. ANPs have high specific surface area and reactivity due to the defects of the bond state, electronic state, and atomic coordination on the surface of nanoparticles. Using ANPs can greatly improve the combustion efficiency, the dynamic and static burning rate of a high-energy condensed system, and the detonation heat and greatly reduce the activation energy of the combustion system. However, these characteristics not only improve the application advantages of ANPs in propellants but also bring difficulties in storage and processing. The newly prepared ANPs are easily oxidized even through spontaneous combustion in an oxidation environment.[1,2]

To improve the surface properties of ANPs, researchers propose a concept of constructing a stable envelope structure on the particle surface. After coating, ANPs have a passivation layer on the surface, which isolates the contact between the external oxidation environment and the active Al atoms. By changing the coating materials, we can get core−shell composite particles with different surface properties. As an important part of solid propellants, nitrocellulose (NC) with high nitrogen content has the characteristics of water resistance, acid and alkali resistance, low cost, and long storage life.[3] Moreover, the NC fiber bundle will undergo the process of swelling to dissolution in the solvent, and the molecular chain is dispersed in the solvent to form a homogeneous sol. Therefore, preparing stable structure core−shell composite aluminum particles with NC sol is of great significance for the storage of ANPs and their application in propellants.[4]

Most researchers used experimental methods to study NC/ANP composite particles. Zachariah et al. from the University of Maryland carried out a large number of studies on Al-NC composite particles prepared by the electrostatic spray method.[5] They found that the combustion efficiency of Al-NC composite particles prepared by the electrostatic spray method was basically equivalent to that of nonagglomerated nano aluminum powder in combustion performance. When the mass fraction of NC was increased from 3 to 10%, the ignition
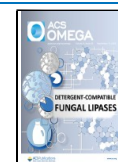
delay time was shortened from 3.5 to 0.3 ms, and the combustion time was prolonged from 46 to 64 ms, respectively. Wang et al. successfully prepared gel-like NC/ANP composite particles by the electrostatic spray method,[6] and the mass fraction of NC was 1−10%. The combustion performance test showed that the gel-like NC/ANP composite particles had stronger combustion behavior than ANPs, and 10% NC/ANP composite particles showed the longest combustion time (∼64 ms) and the shortest ignition delay time (∼0.26 ms). Yan et al. prepared uniformly sized and porous NC/ANP microspheres by the electrostatic spray method. The NC/ANP microspheres had high pressurization and combustion propagation rates.[4]

Molecular dynamics (MD) simulations are an effective theoretical research means from the atomic scale. They have been successfully applied to explore the properties of ANPs. Alavi used MD simulations to predict the melting points of ANPs, and the simulation results were in agreement with the experimental results.[7] Much work has been devoted to exploring the sintering of metal nanoparticles by molecular dynamics (MD) simulations.[8−13] Koraychy et al. studied the coalescence and surface deposition process of two Al and Ni nanoparticles.[8] They found that the degree of coalescence and deposition was strongly temperature dependent, and the deposition rate increases with the temperature, while the sintering and deposition of heteronanoparticles are more significant at lower temperatures than melting. Song and Wen studied two different sizes of nickel nanoparticles through MD simulations[12] and found that the sintering of two different sizes of nanoparticles occurred in three stages closely related to surface melting. Liu et al. simulated the nonequilibrium molecular dynamics of the combustion of nano-Al particles coated with ethanol/ether molecules[14] and explored the combustion mechanism of coated ANPs. Wang et al. optimized the preparation process of core−shell Al/Viton A composite particles and gained insights into the effect of Viton A on the combustion of aluminum particles with MD simulations.[15] They found that Viton A could decompose and react with Al_2O_3 and destroy the dense Al_2O_3 shell during heating. At the same time, the addition of Viton A led to a higher completion degree of the reaction of the core Al and oxygen, and the sintering of the Al particles was also decreased.

As far as we know, the research of NC and nano aluminum powder mixture systems is mostly based on experimental methods, which makes it difficult to directly detect the reaction process and microscopic mechanism in the rapid response stage. In order to explore the ignition and combustion mechanism of NC/ethanol/ether-coated ANPs, MD simulations are carried out on three different models in this research. Radial distribution function (RDF), average displacement, mean square displacement (MSD), and other parameters will be quantitatively characterized to reveal the ignition and combustion mechanism of NC/ethanol/ether ternary-coated ANPs for the first time. This reveals the possible reasons why the ternary coating increases the burning time and efficiency of ANPs. Therefore, it will be of great significance to study the combustion of ANPs following coating with organic materials.

2. MATERIALS AND METHODS

2.1. ReaxFF-lg Long-Range Correction Reaction Force Field.
In the current work, MD simulations are performed using a large-scale parallel atom/molecule simulator

(LAMMPS[16]), and visualization postprocessing is performed using VMD[17] and OVITO[18] software. The core of the MD simulations is the force field. Reasonable force field parameters greatly affect the accuracy and results of simulations. ReaxFF interatomic potential is a reaction force field based on bond order (BO), which has been successfully applied to computational chemistry.[19] In this paper, the ReaxFF force field used comes from Mei et al.[20] Different from the concept of atomic type in the classical force field, ReaxFF adopts bond order (BO) formalism to evaluate the interactions between atoms including bond and long-range pair interactions. Equation 1 presents the total energy in the ReaxFF force field[14]

$$E_{system} = E_{bond} + E_{over} + E_{under} + E_{lp} + E_{val} + E_{tors} \\ + E_{vdWaals} + E_{Coulomb}$$ (1)

where E_{system} denotes the total energy of the system. The bond (E_{bond}), over coordination (E_{over}), undercoordination (E_{under}), lone pair (E_{lp}), valence angle (E_{val}), dihedral twist angle (E_{tors}), van der Waals ($E_{vdWaals}$), and Coulomb ($E_{Coulomb}$) energy terms contribute to the total energy to varying degrees. In addition, $E_{vdWaals}$ and $E_{Coulomb}$ are nonbonding terms, and other energies are expressed through BO.

However, the first principle based on density functional theory (DFT) is often used to fit the results in the development of the ReaxFF reaction force field. This method will underestimate the van der Waals force of nonbonding molecules in the calculation process. Therefore, the ReaxFF reaction force field usually underestimates the calculation of equilibrium density when describing molecular systems.[21] In addition, the expression of the ReaxFF force field has included the expression of van der Waals interaction. Therefore, it is necessary to introduce a new nonbonding term without affecting the fracture and formation of chemical bonds in the molecule, so that the ReaxFF force field can correct the long-range force and reduce the impact on covalent bonds. Liu and Goddard used a low-gradient model (Low-Gradient) to correct the long-range effect of density functional calculations.[22] Based on this, the ReaxFF-lg long-range correction reaction force field is developed by using a similar model to correct the long-range effect of the ReaxFF force field. Here, we use the ReaxFF-lg long-range correction reaction force field for the simulation calculation. The expression of total energy in the ReaxFF-lg force field is described by eq 2

$$E_{system}^{lg} = E_{system} + E_{lg}$$ (2)

where E_{lg} denotes the lg long-range amendments. Its calculation uses the Low-Gradient model. Equation 3 is the calculation formula of E_{lg}

$$E_{lg} = -\sum_{ij,i<j}^{N} \frac{C_{lg,ij}}{r_{ij}^6 + d \cdot R_{eij}^6}$$ (3)

where r_{ij} is the distance between atoms i and j; R_{eij} is the van der Waals interaction equilibrium distance between atoms i and j; $C_{lg,ij}$ is the correction coefficient of dispersion force; and d is the scale factor.

2.2. Simulation System and Setup.
This study includes two simulation scenarios. For the study on the pyrolysis mechanism of the NC single chain discussed in Section 3.1, the simulation box has dimensions of 25.792 Å × 25.792 Å × 25.792 Å, and the density of the NC system is set to be 1.6 g/
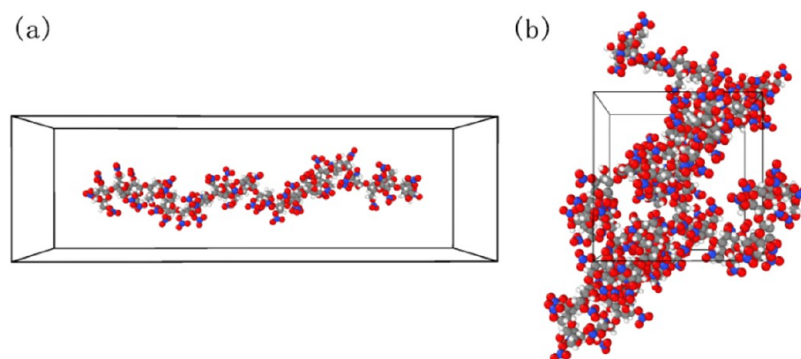
Figure 1. (a) NC single molecular chain model. (b) NC amorphous cell pyrolysis simulation snapshot of the initial configuration structure.
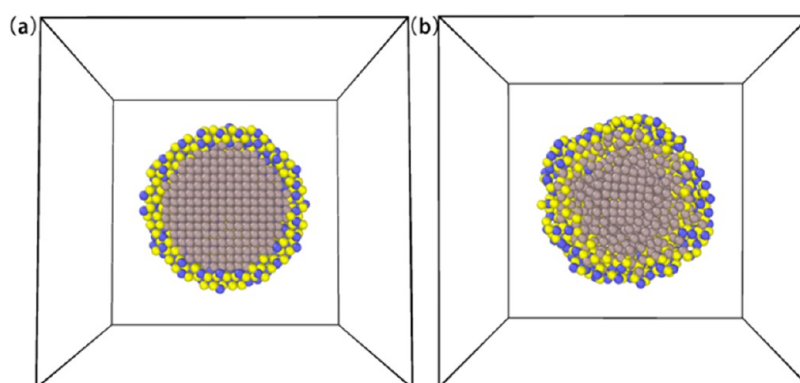

Figure 2. (a) Initial configuration and (b) optimized configuration of core−shell ANPs used in this paper. The Al core diameter is 4 nm and the thickness of the oxide shell is 0.5 Å. Atoms are colored by atom type: blue and dark gray for shell and core Al atoms, respectively, and yellow for O atoms.
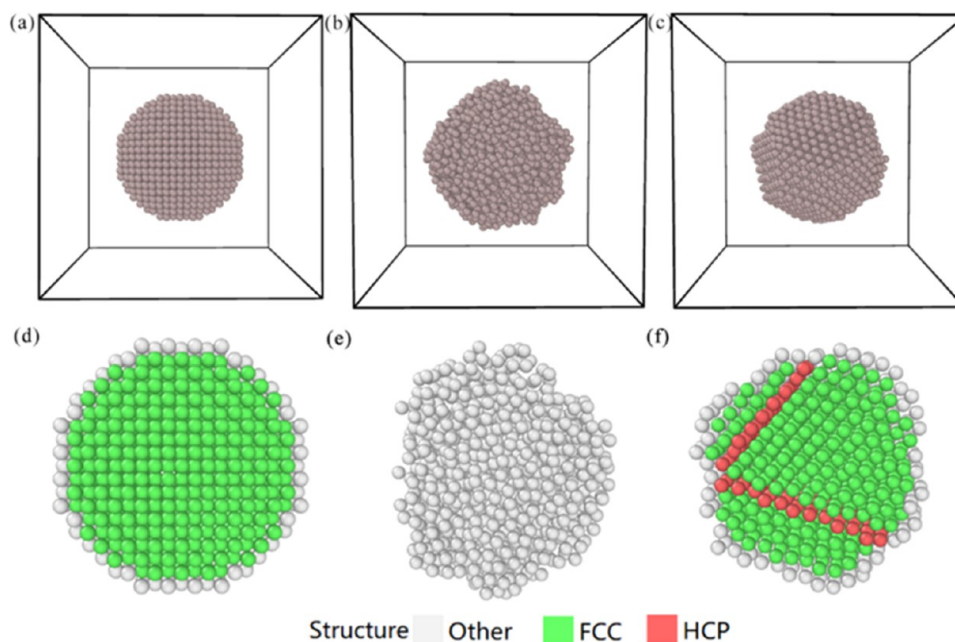

Figure 3. (a) Initial model, (b) melting model, (c) particle configuration of the annealing model. (d) Initial model, (e) melting model, and (f) crystal type distribution of particle center section of the annealing model.

cm^3, which is close to the actual density. Figure 1(a) shows an NC single molecular chain model, and Figure 1(b) shows the initial configuration snapshot of amorphous cell pyrolysis. The thermodynamic process of the system is as follows. First, every atom is assigned a velocity to the specified temperature of 250

K in a Gaussian distribution, following which the system is relaxed under the canonical ensemble (NVT) at 250 K for 1 ps to obtain a reasonable configuration. Then, the system temperature is increased to 3000 K slowly at a heating rate of 0.03 K/fs, finally lasting for 100 ps at 3000 K. The pyrolysis
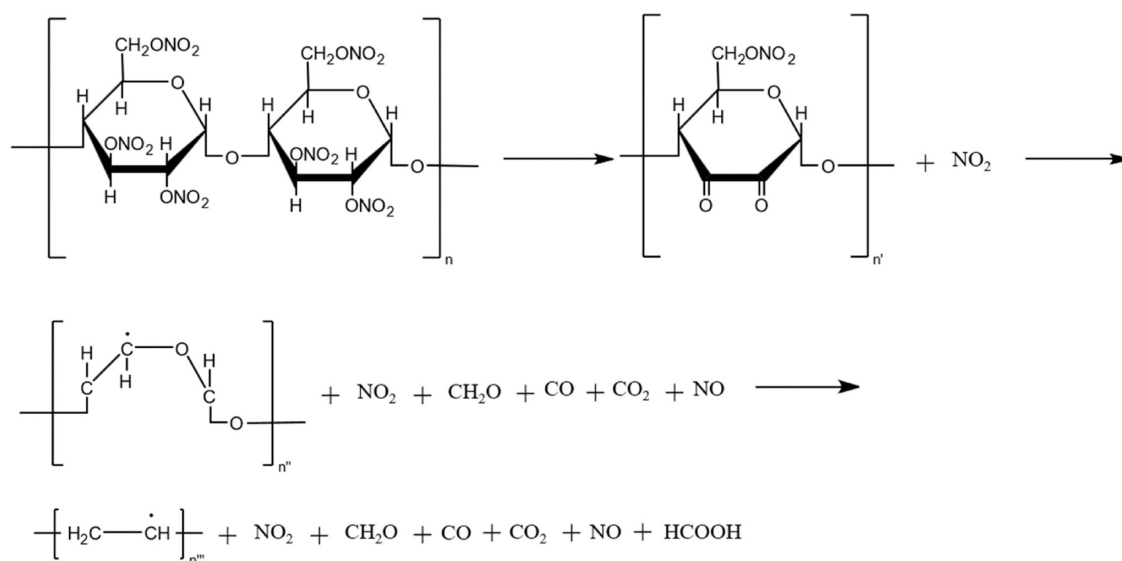
Figure 4. Pyrolysis process of the NC single molecular chain model.

reaction starts in the heating phase (about 1182 K). Berendsen[23] control theory was used to control the temperature with 20 fs of the temperature resistance coefficient. The time step is 0.2 fs, which is enough for the simulation.

For the cases of preparing and burning the ANPs, we use three ANPs models, which are sANPs, csANPs, and cANPs. The simulation box has dimensions of 110 Å × 110 Å × 110 Å, ANPs are located in the center of the box, and other molecules such as NC, ethanol, ether, and oxygen are randomly distributed around ANPs. In our study, the ANP has a typical core–shell structure, in which the Al core diameter is 4 nm and the oxide shell thickness is 0.5 nm. According to Liu et al., the melting point of ANPs changes linearly with diameter when the diameter is more than 2 nm.[24] Considering the computational cost, 4 nm ANPs are sufficient to show thermodynamic properties. The Al core and alumina shell models are cut from cubic crystals and assembled together. The fusion process ensures close contact between the core and shell and eliminates surface stress. The basic idea is to relax the passivated particles at 50 K for 1.5 ps to obtain the stable configuration at this temperature; then, the particles are heated to 300 K at a heating rate of 10^{13} K/fs under the NVT ensemble, and the shell–core structure gradually integrates during this process. Finally, the passivated particles are relaxed for 200 ps at 300 K to obtain a stable configuration at room temperature. Figure 2 shows the initial configuration and optimized configuration of the passivated ANPs.

In order to establish the cANPs model, we first need to obtain the annealed ANPs model. ANPs constructed directly by script commands in LAMMMPS are ideal spherical particles composed of face-centered cubic (FCC) cells. To eliminate the edge effect of ANPs, annealing and recrystallization are necessary. The basic idea is to cut out an aluminum particle with a diameter of 4 nm in the aluminum FCC crystal block, and the whole particles are relaxed at 1300 K to completely melt. Then, to obtain the annealed ANPs at 300 K as the initial model for the subsequent simulation, the molten aluminum clusters are cooled and recrystallized. The whole annealing process is carried out under the NVT with an embedded atom method (EAM) force field. The Verlet integral algorithm was used to solve the Newton motion equation. The Nose–

Hoover[25] theory was used to control the temperature. The temperature damping coefficient is selected as 100 fs. The accuracy and efficiency of recrystallization annealing are related to the selection of the simulated force field and cooling rate. In our study, we choose 20 K/ns as the cooling rate, and the cooling rate is also verified to have good accuracy and economy.[26] Figure 3 shows the ANPs model before and after annealing and the crystal type distribution of the central section.

3. RESULTS AND DISCUSSION

3.1. Force Field Verification of the NC Thermal Decomposition Mechanism. The force field used in this study has been proven to be effective for the ethanol–ether–oxygen system.[14] However, NC molecules are quite different from ethanol and ether molecules. The chemical properties of ethanol are determined by hydroxyl groups, and ether is characterized by its self-propagating autoxidation (peroxidation) process.[27] However, NC molecules will undergo severe self-decomposition at higher temperatures (573 K), and the decomposition products are complex. Therefore, it is necessary to simulate the thermal decomposition mechanism of NC molecules in the ReaxFF MD simulations. The thermal decomposition reaction simulation settings are shown in Section 2.2.

The thermal decomposition temperature of the NC single chain is about 1182 K during the heating process,[28] which is obviously higher than the experimental temperature. This is because the thermal decomposition of NC is limited by the time scale of ReaxFF MD simulations, which has been confirmed in a large number of literature studies.[29−31] Figures 4 and 5 show the pyrolysis process and the variation curve of the number of key product molecules with time in the thermal decomposition process of the NC single molecular chain model. The first gas phase product is NO_2, which is consistent with the fact that the $-NO_2$ base strength measured in the heating process of the NC thermal decomposition experiment decreases first. In addition, we find that CH_2O is generated later than NO_2 because CH_2O is the decomposition product of the $O-NO_2$ group on the primary C-6 position. To see this process more clearly, Figure 6 shows a snapshot of the local
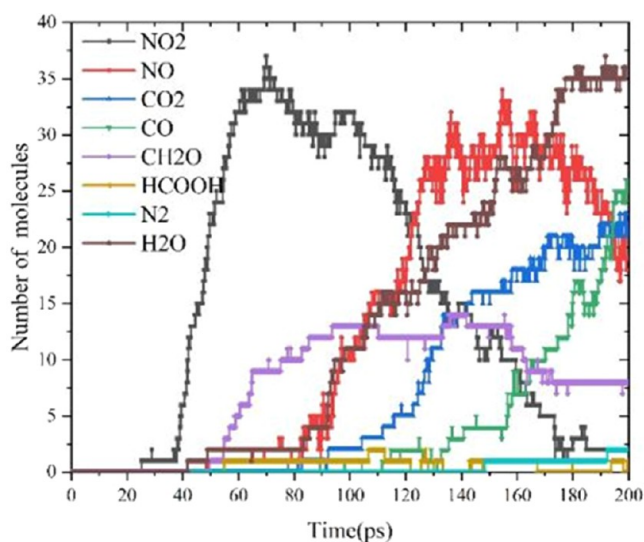
Figure 5. Time-dependent curves of the molecular number of key products during thermal decomposition of the NC single molecular chain model.

structure of the decomposition process of the primary $O-NO_2$ group in the simulation. The fracture of the $O-NO_2$ bond and the subsequent formation of CH_2O can be clearly seen in Figure 6. From Figure 5, we can also find that the number of H_2O, NO, CO_2, and CO molecules begins to increase, and formation of a small amount of HCOOH with the number of NO_2 molecules reaches the peak.

In addition, there are many researchers interested in the fracture of molecular chains during thermal decomposition of NC. Jutier et al. believed that the thermal decomposition of NC did not necessarily lead to the fracture of the chain.[32] However, Wang et al. believed that along with the denitrification process, the NC macromolecular chain would be decomposed into small molecules. In our study, we capture the fracture of the $C-O-C$ bond in NC molecular chains, as shown in Figure 7. In the pyrolysis process of the NC single molecular chain model, the interannular $C-O-C$ bond will be broken, and NC is decomposed into small molecules from macromolecular chains. However, the $C-O-C$ bond breakage in the NC molecular chain is relatively lagging behind, which supports Wang's view that NC macromolecular chains will be decomposed into small molecules along with the denitrification process. It also verifies the accuracy of using the ReaxFF force field to simulate the NC system.

3.2. Preparation of ANPs with NC/Ethanol/Ether. As for the establishment of the NC/ethanol/ether ternary coating

ANPs model, the simulation box has dimensions of 120 Å × 120 Å × 120 Å. The annealed and passivated ANPs established in Section 2.2 are placed in the center of the box, and the ethanol ether solution molecules are placed in the surrounding area of ANPs. In addition, a vacuum region of 7 Å is set between NC/ethanol/ether solution molecules and ANPs as a buffer region. The volume ratio of ethanol molecules to ether molecules in the NC/ethanol/ether solution is 1:1. Considering that the ANPs used in our study are small, the number of molecules in the NC/ethanol/ether solution needs to be limited within the range that ANPs can withstand, otherwise ANPs are prone to deformation. The specific values are listed in Table 1. The position distribution of ethanol ether solution molecules is completed by the Packmol program,[33] so that it initially forms a nearly uniform mixed solution system.

The whole simulation process is carried out under the NVT ensemble. The ANP temperature is set at 300 K, which can ignore the thermal vibration of the base atom. All aluminum atoms can retain interaction with other atoms while fixing the site. The temperature of the NC molecular chain is selected as 300 K to ensure the structural stability of the NC molecular chain. The temperature of ethanol ether solution is selected as 500 K, and the higher solution temperature can make up for the limitation of time scale, helping us get simulation results similar to those in the experiment (time scale: milliseconds) within a reasonable time range (time scale: ps). According to the study of Liu et al., 500 K almost never breaks the results of organic molecules at short times[14] and can effectively inhibit the formation of hydrogen bonds, which is conducive to the development of coating. Berendsen control theory, which is similar to a hot bath, is used in temperature control. The temperature damping coefficient is set to 25 fs. In consideration of the possible dissociation and bonding in the coating process, the time step is 0.25 fs, and the whole simulation lasts 100 ps.

Figure 8 shows the molecular isothermal adsorption curve of NC/ethanol/ether solution coating-annealed ANPs and -passivated ANPs. In the coating process of passivated ANPs, the adsorption rates of ethanol and ether molecules are always slower than those of annealed ANPs. At the end of the coating, the number of ethanol molecules in the coating layer on the particle surface is about 287, the number of ether molecules is 135, and the ratio of ethanol/ether molecules is about 2.12. The number of ethanol ether molecules in the coating layer of passivated ANPs is significantly less than that of annealed ANPs, indicating that the compactness of the coating layer on the surface of passivated ANPs is relatively poor.

In the actual production process, after ANP particles and the solution are fully mixed, more organic solutions are removed in
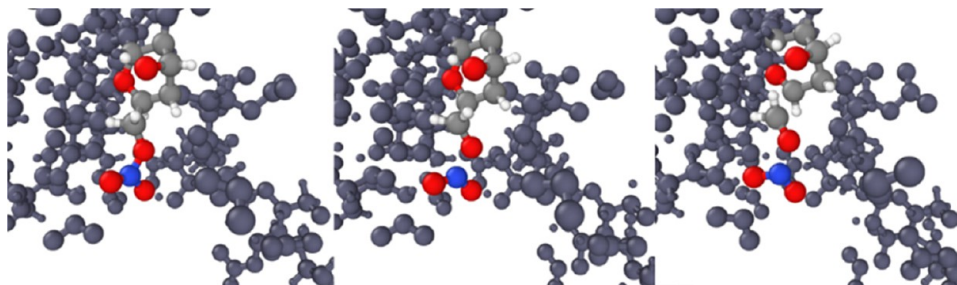

Figure 6. Snapshot of the thermal decomposition process of the $O-NO_2$ bond. Atoms are colored by atom type: blue for N atoms; red for O atoms; white for H atoms; gray for C atoms; and black for other atoms (out of focus).
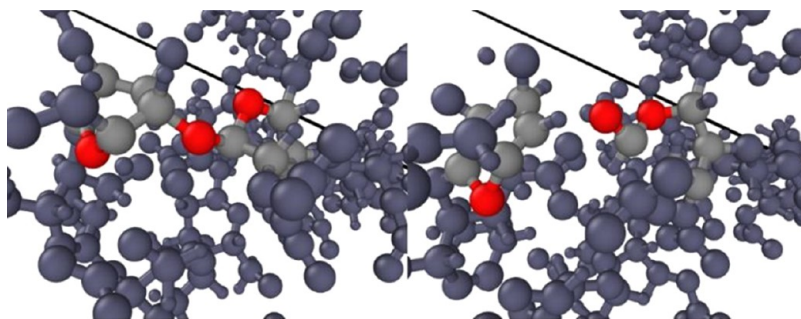
Figure 7. Snapshot of C−O−C bond decomposition over the local structure in the thermal decomposition process of the NC single-chain model.

Table 1. NC−Alcohol Ether Solution Molecular Number for sANPs, csANPs, and cANPs

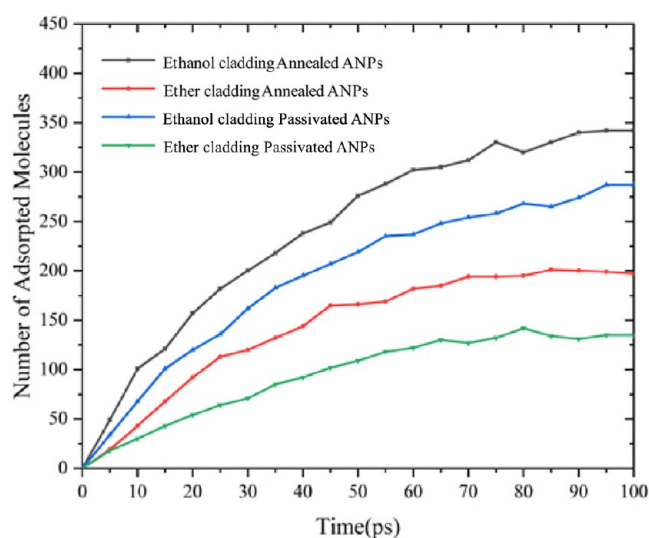|	NC	ethanol	ether
sANPs	0	0	0
csANPs	3	1000	562
cANPs	3	1000	562

Figure 8. Molecular isothermal adsorption curves during annealing and passivation of ANPs coated with NC/ethanol/ether solution.

the oven. Therefore, at the end of the cycle coating process, an evaporation elimination procedure is carried out to eliminate atoms that are not tightly adsorbed on the ANPs. Considering that the real ignition environment is about 300 K, the evaporation elimination simulation is carried out at 300 K. For the first time, a manual filter is selected to remove the free complete solvent molecules in the box. Then, the filtered ANPs are put in the center of a cube box of 120 Å × 120 Å × 120 Å, and to leave sufficient space for the release pressure of the coating layer, the environment is set as vacuum. After each filtering simulation, the separated solvent molecules are filtered until no molecules are separated, and the cycle ends.

Figure 9 shows the molecular numbers of each component in the coating layer after each filtering of cANP and csANP. From Figure 8, we can find that, whether csANP or cANP, a large number of ether molecules and a small amount of ethanol molecules are separated from the filtering simulation, and NC molecules remain stable. Because of different molecular structures and adsorption modes, ethanol is chemically adsorbed, while ether is physically adsorbed, and ether molecules are more likely to escape in a dry environment. The final composite particles are shown in Figure 10.

In order to explore the relative structure between the organic coating layer and ANPs, Figure 11 shows the cross-sectional charge distribution and atomic potential energy distribution of the final configuration of cANPs. The Al atoms on the surface of ANPs are strongly positively charged, while the ethanol ether molecules infiltrated into the surface of ANPs are strongly negatively charged. A new bond pair is formed between the Al atoms on the particle surface and the ethanol
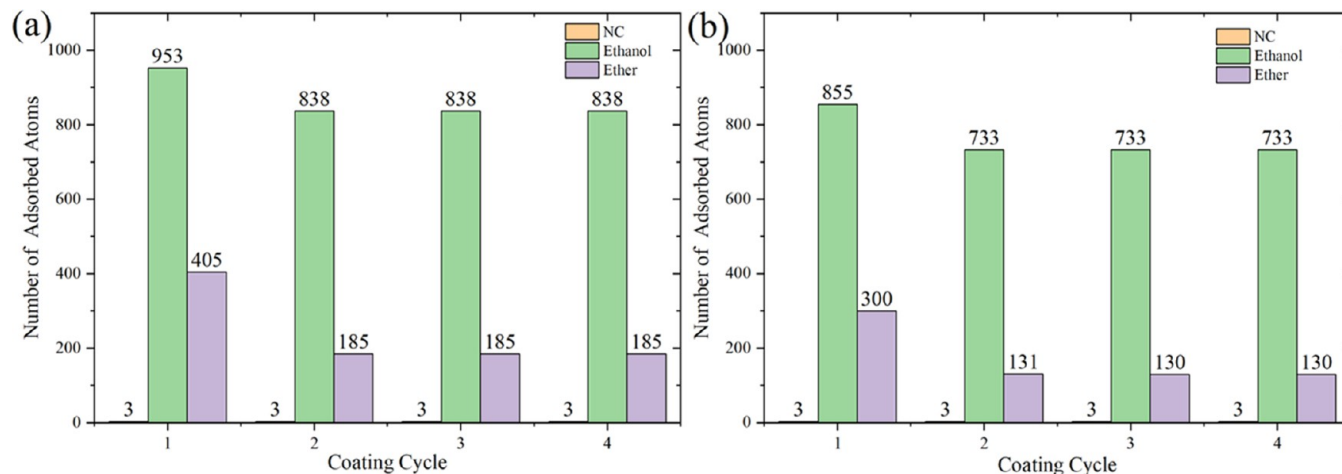

Figure 9. (a) cANP and (b) csANP filter out the molecular number of each component in the simulated envelope each time.
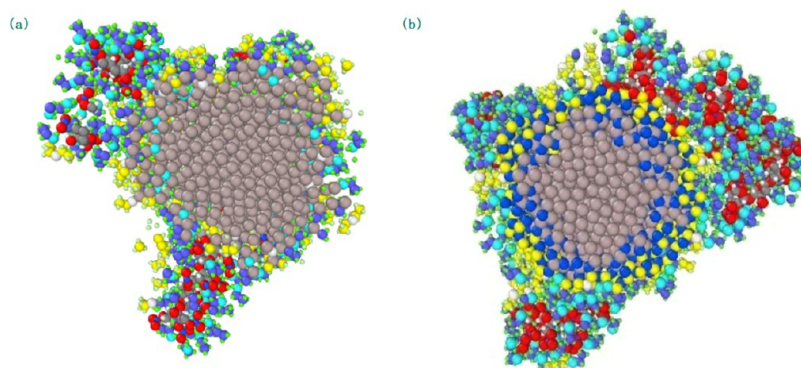
Figure 10. (a) cANP and (b) csANP final configurations. Atoms are colored by atom type: light gray for core Al atoms; yellow and blue for oxide layer O and Al atoms, respectively; dark gray, purple, red, and green for NC C, N, O, and H atoms, respectively; bright yellow, white, and grass green for ethanol/ether C, O, and H atoms, respectively.
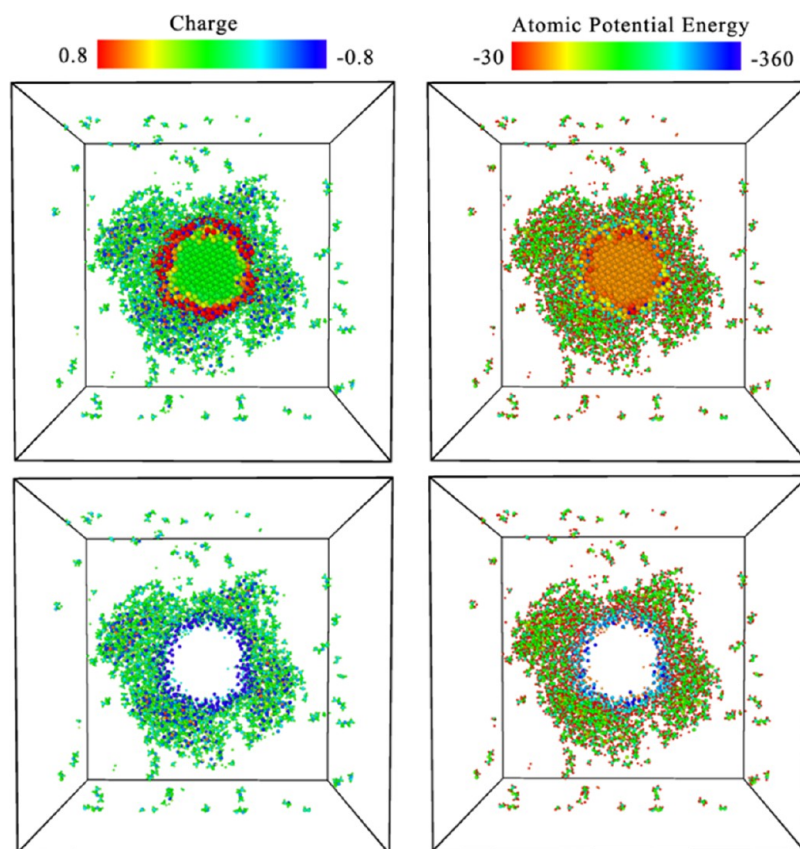

Figure 11. Charge coloring diagram and atomic potential energy coloring diagram of the central section of cANPs' final configuration.

ether molecules, and the charge transfer also occurs between the bonding atoms. Therefore, this layer is a chemical adsorption layer. From Figure 11, we can also find that the atomic potential energy of the NC/ethanol/ether solution in the chemical adsorption layer is low and the adsorption configuration is more stable. The outside ethanol ether molecule has a weak charge, indicating that the molecules outside the coating layer interact through nonbonding forces such as van der Waals force and Coulomb force, so this layer is a physical adsorption layer. The atomic potential energy in the physical cladding layer is high, and the structure is relatively unstable. NC/ethanol/ether solution is still the result of the combination of physical adsorption and chemical adsorption. In addition, the O and N atoms in the NC molecular chain also

have strong charge values, which also reveals the hydrogen bond between the ethanol ether molecule and the NC molecular chain.

We calculate the radial distribution functions of different atom pairs, as shown in Figure 12, to quantitatively study hydrogen bonding between the surface structure of ANPs and the NC/ethanol/ether solution of the final configuration ANPs. From Figure 12 (a), we can find that the surface O atoms of ANPs are mostly located near the Al atom, about 1.95 Å, indicating that the outermost Al atoms of ANPs tend to form an alumina layer provided by organic inclusion. The peak value of g (Al−NO) is relatively low, and the first peak is located near 1.8 Å, indicating that the part of the NC molecular chain involved in chemical adsorption is less, and it
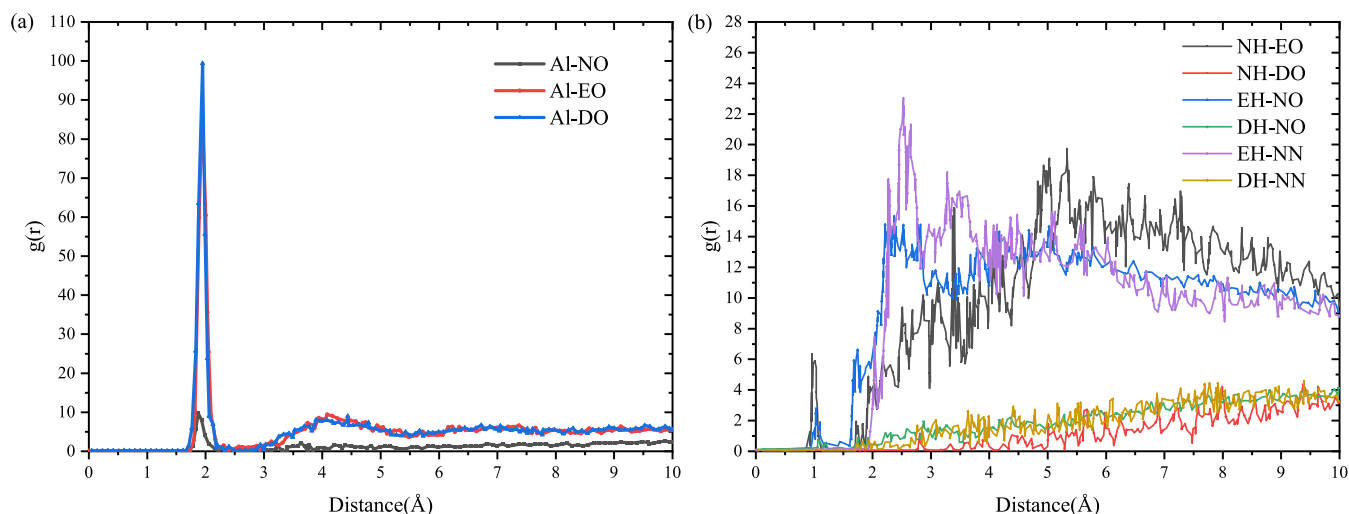
Figure 12. Radial distribution function curves of related atom pairs in the cANP final configuration. (a) Al−NO, Al−EO, and Al−DO atom pairs. (b) NH−EO, NH−DO, EH−NO, DH−NO, EH−NN, and DH−NN atom pairs. NO: the O atom in the NC molecular chain, EO: the O atom in ethanol molecules, DO: the O atom in ether molecules, NE: the H atom in the NC molecular chain, EE: the H atom in ethanol molecules, DE: the H atom in ether molecules, and NN: the N atom in the NC molecular chain.

is more inclined to adsorb on the surface of ANPs by chemical adsorption at one end or one section of the molecular chain. The adsorption strength is stronger than that of ethanol ether molecules. The other segments are adsorbed on the surface of ANPs by physical adsorption through the traction of the chemical adsorption section and hydrogen bonding. Figure 12 calculates the radial distribution function of H−O and H−N atomic pairs between NC molecular chains and ethanol ether molecules. From Figure 12(b), we can find that the ethanol molecules are more likely to attract each other with NC molecular chains. The reason is that polar −OH in the ethanol molecule and the polar −OH and −ONO$_2$ groups in the NC molecular chain are more likely to attract through the Coulomb interaction. Ether molecules are not easy to attract in the NC molecular chain, which can prevent large agglomeration and make the NC molecular chain dissolve smoothly to form a homogeneous solution.

To analyze the adsorption behavior of NC molecular chains on the surface of csANPs intuitively, Figure 13 is a structural snapshot of the final configuration of csANPs. The −NO$_2$ and −OH groups in the NC molecular chain pull the chain link to
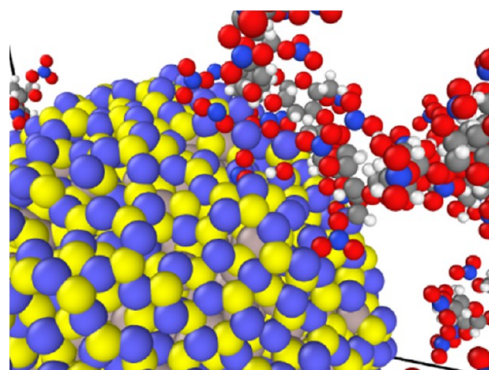

Figure 13. Local patterns of NC adsorption in the simulated final configurations of csANPs. Atoms are colored by atom type: dark gray for core Al atoms; yellow and purple for oxide layer O and Al atoms, respectively; light gray, blue, red, and white for NC C, N, O, and H atoms, respectively.

adsorb to the surface of passivated ANPs, accompanied by the detachment of the −NO$_2$ and −OH groups. The atoms in the detached −NO$_2$ and −OH groups will not be further separated, and it is difficult to penetrate the interior of passivated ANPs. Therefore, NC molecular chains are still adsorbed on the surface of passivated ANPs by physical and chemical adsorption.

Active Al atoms are the main reactants of fuel. After the ANPs are completely coated, the content of active Al is a very important detection index. Table 2 shows the content of active

Table 2. Al Atomic Activity for sANPs, csANPs, and cANPs

	active Al atom (%)	partially oxidized Al atom (%)	oxidation Al atom (%)
sANPs	27.4	42.6	30.0
csANPs	22.1	51.8	26.1
cANPs	52.00	38.20	9.80

Al atoms in the three models. According to the oxidation degree of the Al atom, we divide it into an active Al atom, a partially oxidized Al atom, and an oxidation Al atom. For passivated ANPs, the Al atom with a charge less than the average charge in the core region is defined as the active Al atom; the Al atom whose charge is more than the average charge in the shell is defined as the oxidation Al atom; and the AI atom with the charge between the average charge in the core and shell regions is defined as the partially oxidized Al atom. For the cANPs model, since there is no passivation treatment and the concept of average shell charge is not available, the Al atom whose charge is less than 0.5 is defined as an active Al atom. An Al atom with a charge of more than 1 is defined as an oxidized Al atom. An Al atom with a charge between 0.5 and 1 is defined as a partially oxidized Al atom. Table 2 shows that NC/ethanol/ether coating treatment could reduce the content of the oxidation Al atom. However, no matter which model, the total content of unoxidized and partially oxidized Al atoms is above 70%.

3.3. MD Simulations of Heating and Combustion Processes. *3.3.1. Heating Period.* After the evaporation elimination procedure, the ignition and combustion stages can
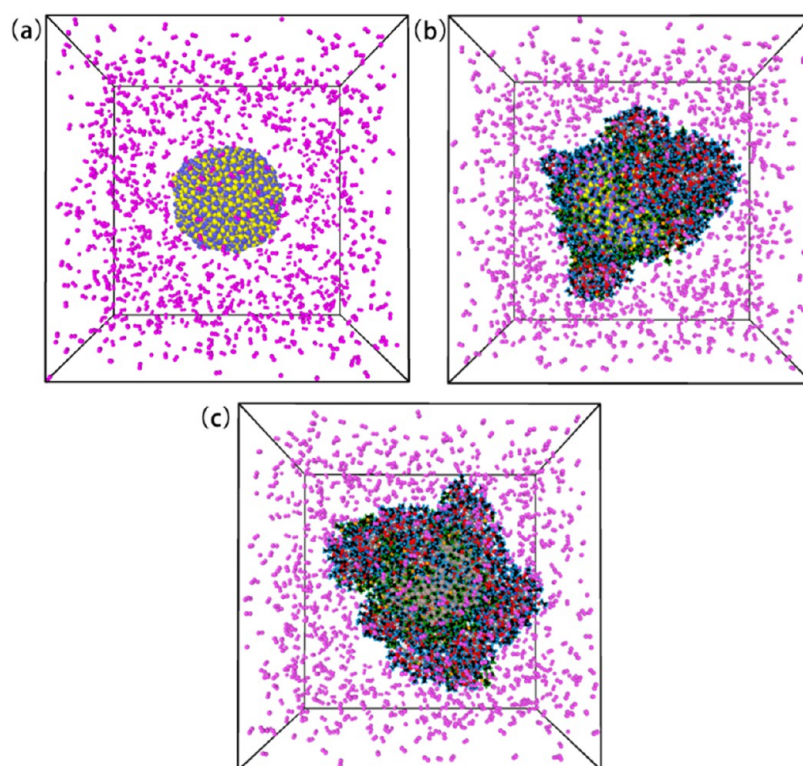
Figure 14. Initial models of the heating period: (a) sANPs, (b) csANPs, and (c) cANPs.
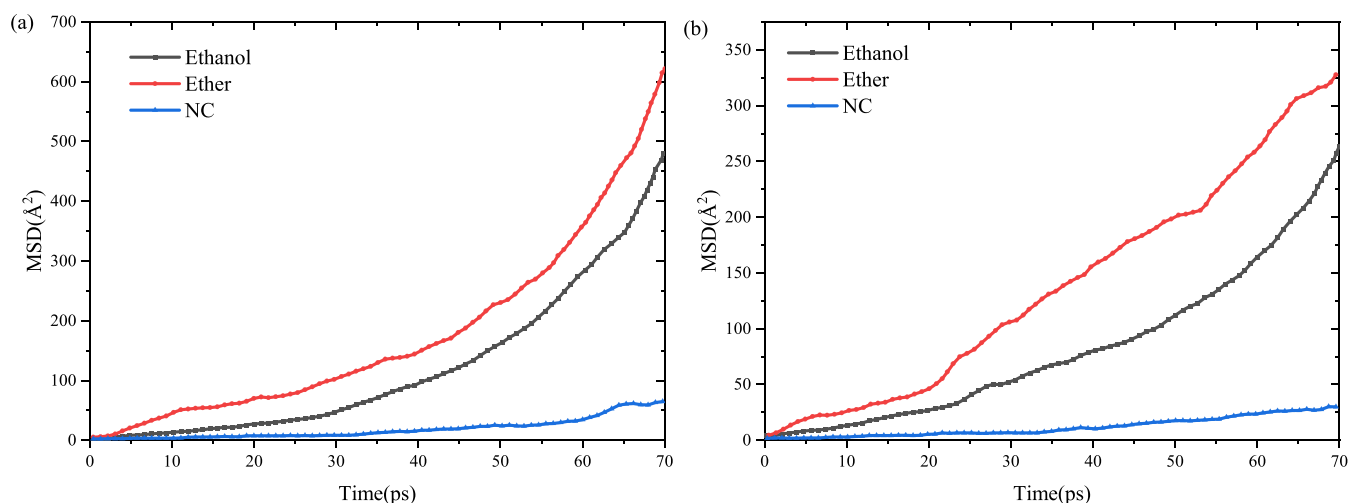

Figure 15. (a) csANPs and (b) cANPs mean square displacement curve of components in the heating period.

be carried out. In order to verify the effect of the NC/ethanol/ether coating layer on the heating performance of ANPs, we set up three combustion models of sANPs, csANPs, and cANPs. In the heating period, the three ANPs models are put in a 110 Å × 110 Å × 110 Å box, and 1200 O_2 molecules are randomly put around the ANPs. Figure 14 shows the three initial models used in the heating period. The specific parameters of the heating model are as follows: First, the heating system is relaxed at 300 K, and then the system temperature is increased to 1000 K in 70 ps under the NVT ensemble. The defined rate of heating is 10 K/ps. According to the ignition characteristics of ANPs, 1000 K is enough to ignite ANPs.[34]

At present, although there are many controversies about the ignition mechanism of ANPs, the diffusion movement of atoms is considered to be one of the important ideas about the ignition mechanism of ANPs.[35,36] Figure 15 calculates the mean square displacement curves of ethanol, ether, and NC atoms during the heating period of csANPs and cANPs. At the initial heating period (−20 ps), the atomic mobility of each component increases slowly, and the coating layer does not parse clearly at low temperatures. After 20 ps, the atomic mobility of ether and ethanol begins to increase rapidly. At this time, the ether and ethanol molecules begin to parse and diffuse rapidly, while the parsing and diffusion of NC lag significantly. In addition, ether molecules show higher mobility during ignition, indicating that the parsing and diffusion of ether are earlier than those of ethanol. Due to the strong physical adsorption in the csANP coating layer, csANP coating layer atoms have higher mobility than cANPs.
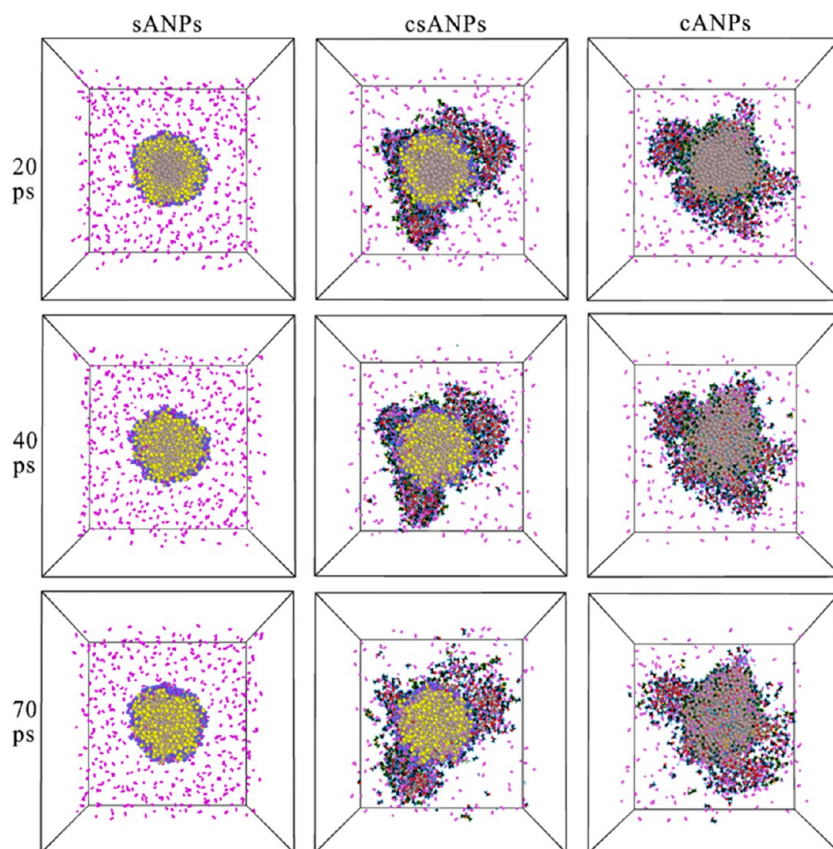
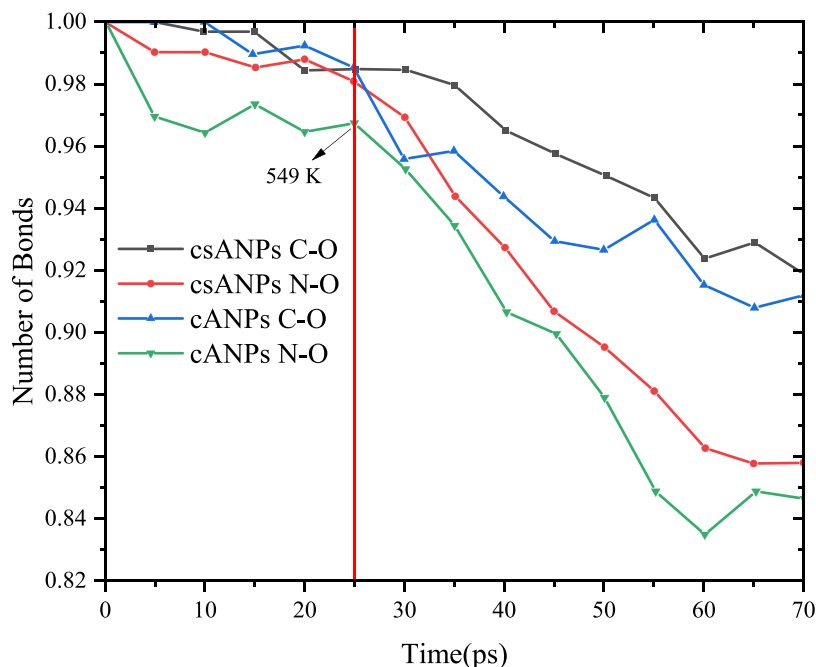**Figure 16.** sANPs, csANPs, and cANPs configuration diagram of the central section during the heating period.

Figure 17. Change rate curves of C−O and N−O bond pairs with time during the NC ignition process in csANPs and cANPs models (have normalized values).

In order to observe the diffusion movement of each component atom intuitively in the heating period, Figure 16 shows the central section configuration diagram of sANPs, csANPs, and cANPs systems at different ignition times. At the initial heating period (20 ps), the adsorption of the O_2

molecules on the surface of the ANPs gradually occurred, but it is difficult to penetrate the oxide/coating layer. Because of the coating layer, csANPs and cANPs can adsorb more O_2 molecules around them than sANPs. It means that the organic coating layer is beneficial to the adsorption of the O_2
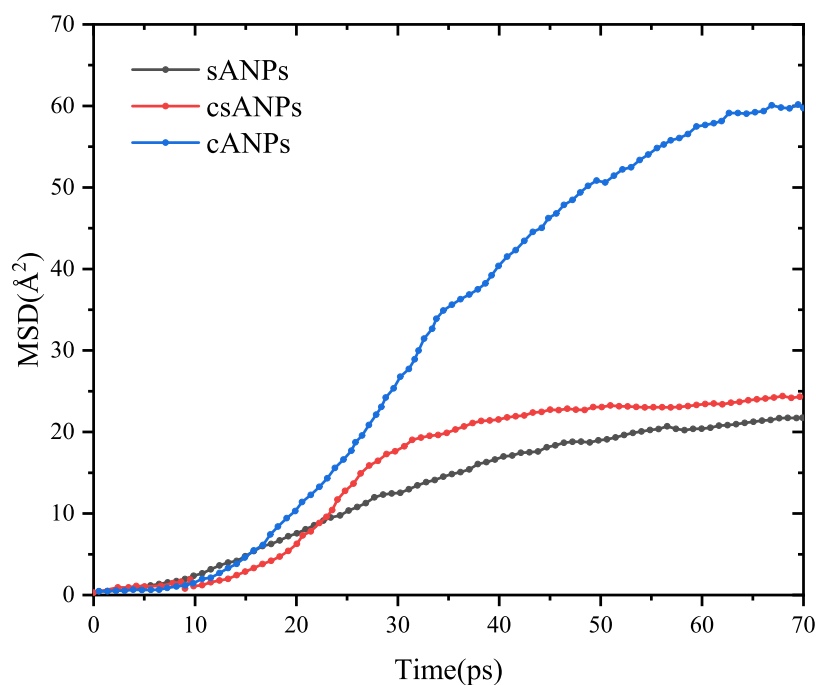
Figure 18. Mean square displacement diagram of the cAl atom during ignition for sANPs, csANPs, and cANPs.
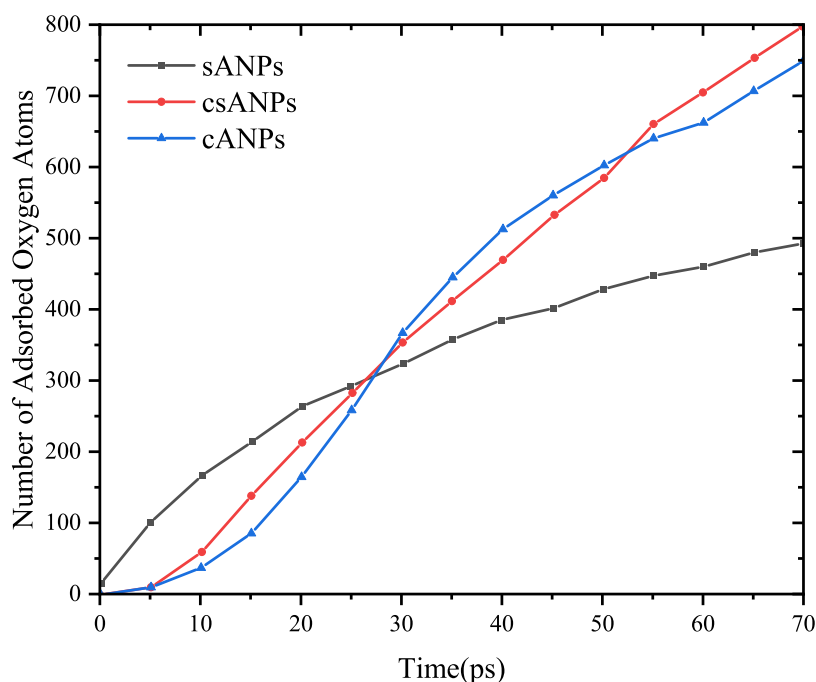

Figure 19. Adsorption quantity of eO atoms changing with time during the heating period for sANPs, csANPs, and cANPs.

molecules. With the increase in temperature (20−40 ps), the Al core atoms begin to melt, and the melting temperature of the Al core decreases significantly. With the melting of the Al core, the O atom in the oxide shell (sO) begins to diffuse inward, while the Al atom in the aluminum core (cAl) begins to diffuse outward. As for cANPs, due to no oxide layer, organic coating layer atoms begin inward diffusing at this stage, which makes the surface structure of ANPs looser. At 40−70 ps, the ethanol and ether molecules in the coating layer are obviously exfoliated, while the NC macromolecular chain is still around the surface of ANPs, although it shows a certain degree of detachment. With the detachment of the coating

layer, the O_2 molecules are further adsorbed on the surface of ANPs, even diffusing into ANPs, which promotes the ignition of ANPs.

The pyrolysis behavior of NC molecular chains during the heating period is also interesting. Figure 17 shows the change rate curves of C−O and N−O bond pairs with time in the heating period of NC (have normalized values). At about 25 ps (549 K), the NC molecular chains in the coating layer of csANPs and cANPs began pyrolysis. NC pyrolysis also releases heat and increases the surface temperature of ANPs, which can shorten the ignition time of ANPs.
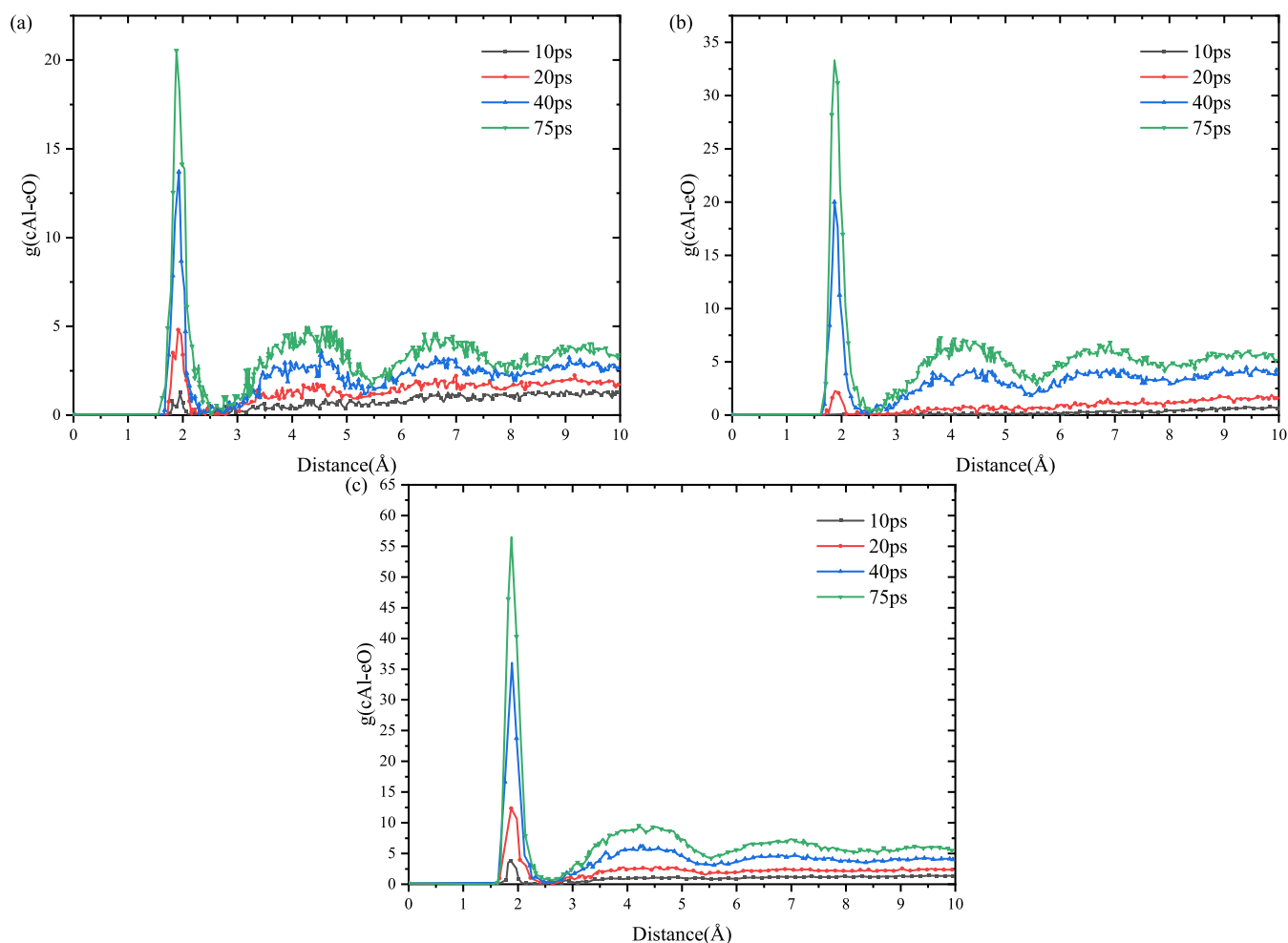
Figure 20. Radial distribution function diagram of the cAl—eO atom pair during the heating period for (a) sANPs, (b) csANPs, and (c) cANPs.

Figure 18 shows the MSD curves of cAl atoms during the heating period of sANPs, csANPs, and cANPs. At the initial ignition stage, the MSD curve of the cAl atom in csANPs and cANPs was lower than that of sANPs, which means that the NC/ethanol/ether coating can improve the stability of active Al core atoms at low temperatures. After that, the MSD curves of cAl atoms in csANPs and cANPs increase rapidly and exceed sANPs at about 22 and 15 ps, respectively. With the increase of temperature, the active Al cores in csANPs and cANPs show higher atomic mobility. High atomic mobility makes the active cAl atoms in ANPs diffuse to the surface and react with external O_2 molecules faster, which also reveals one of the reasons why the NC/ethanol/ether coating layer can shorten the ignition delay of ANPs.

The direct contact reaction of external O_2 molecules with active Al atoms in ANPs is usually considered an important indicator of ANP ignition. Figure 19 shows the variation of the number of O atoms in the range of 2 on the ANP surface during the heating period. At the beginning of ignition, the oxygen adsorption amount of csANPs and cANPs is much lower than that of sANPs. With the increase of temperature, the oxygen adsorption amount of csANPs and cANPs quickly increased and exceeded that of sANPs, which further proves that the NC/ethanol/ether coating inhibits external contact of the O_2 molecules with ANPs at low temperatures and promotes external adsorption of the O_2 molecules and reaction with ANPs at high temperatures.

Figure 20 shows the radial distribution function of the cAl—eO atom during the ignition period. The RDF curves in sANPs, csANPs, and cANPs systems have the same trend over time. As shown in Figure 18, the first peak is about 1.9, corresponding to the Al—O bond length. At 0–20 ps, the first peak value of csANPs is significantly lower than that of sANPs, indicating that the coating inhibits the external contact of the O_2 molecules with Al core atoms at low temperatures. With the increase of temperature, the first peak value of csANPs increases rapidly and exceeds sANPs. It is because at low temperatures, the O_2 molecules adsorbed by the coating layer react rapidly with the reaction sites released on the surface of ANPs after coating layer decomposition, which also reveals another important mechanism of coating layer shortening the ignition delay of ANPs. Finally, with the increase of temperature, the RDF curve appears to have obvious second and third peaks. It shows that the reaction between the O_2 and cAl atoms gradually diffuses inward, forming a long-range ordered oxidation structure.

3.3.2. Combustion Period. In the combustion period, the simulation box is expanded to 150 Å × 150 Å × 150 Å, and the ignition process parameters including the initial models (besides the sizes of the boxes and final temperature) are the same as in Section 3.3.1. Due to the research background being the improvement of aluminum-containing propellants, the combustion temperature of aluminum-containing propellants in the combustion chamber can stabilize at about 3000 K
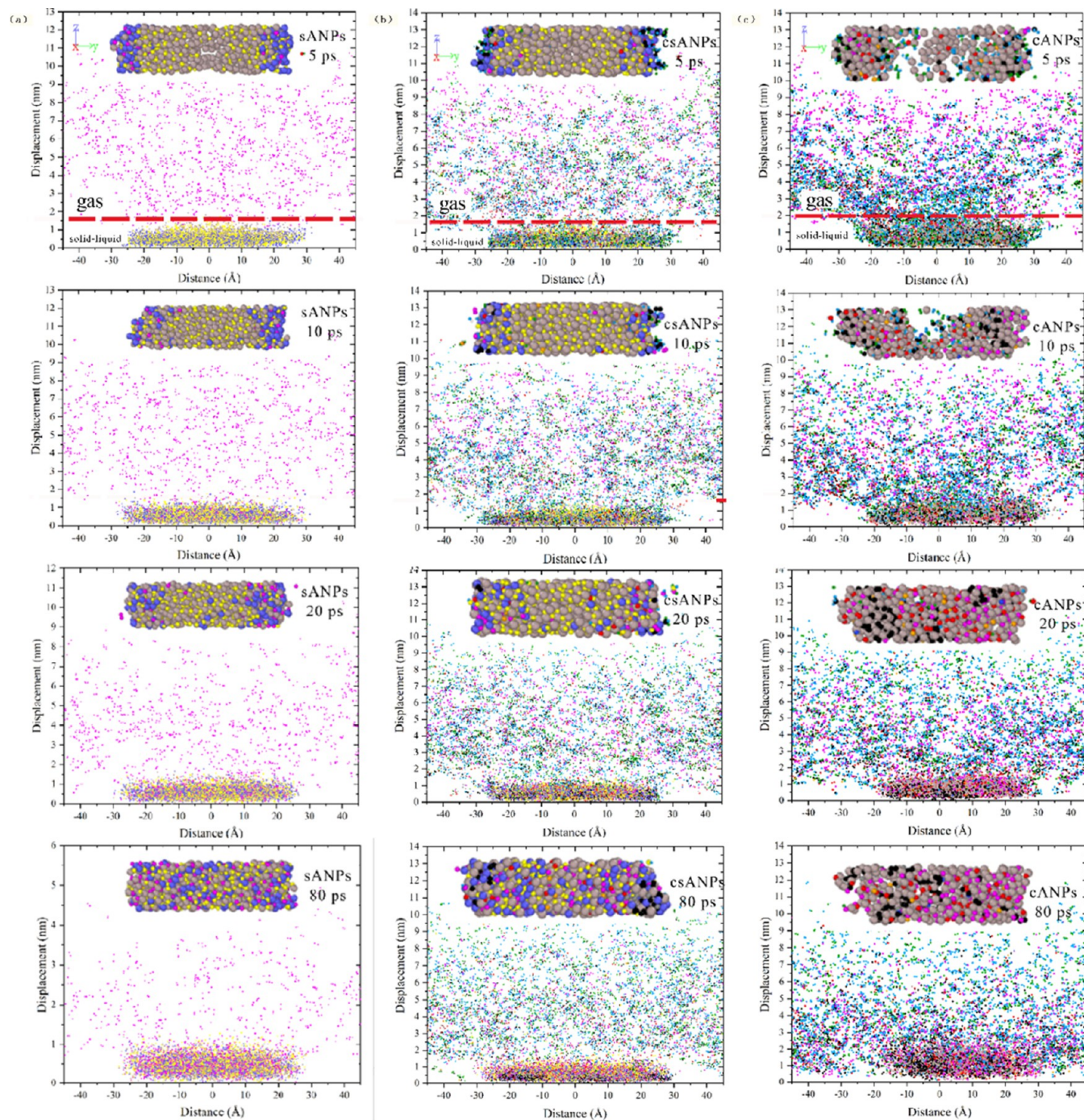
Figure 21. Snapshots of the rectangular central section along the *Y*-axis and the atomic displacement scatter plot during the constant-temperature combustion period. (a) sANPs, (b) csANPs, and (c) cANPs. Atomic coloring by atomic type. Gray: cAl atoms, yellow: O atoms, blue: sAl atoms, black: C atoms, purple: eO atoms, green: H atoms, and red: O atoms.

continuously.[37] To verify the effect of the NC/ethanol/ether coating layer on the combustion performance of ANPs, the temperature of the constant-temperature combustion period is set at 3000 K.

Figure 21 shows the rectangular central cross-sectional views along the *Y*-axis and the atomic displacement scatter plots at different times of the three systems' constant-temperature combustion at different times (with the atomic positions 5 ps before this time as a reference). The central cross-sectional view is shown to better observe the distribution of atoms in ANPs during the combustion stage, and the width of the

rectangular section is 15 Å. The transverse coordinate of the scatter plot corresponds to the radial distribution along the *Y*-axis, and the ordinate represents the absolute displacement of each atom before 5 ps. According to the absolute value of atomic displacement in 5 ps, the displacement scatter diagram of the combustion system can roughly divide into the gas phase and solid−liquid phase regions.

For sANPs and csANPs, because 3000 K is much higher than the melting point of the Al core and the oxide shell, the cAl atom in the central region and the sO atom in the oxide shell diffuse rapidly, and the shell−core structure completely
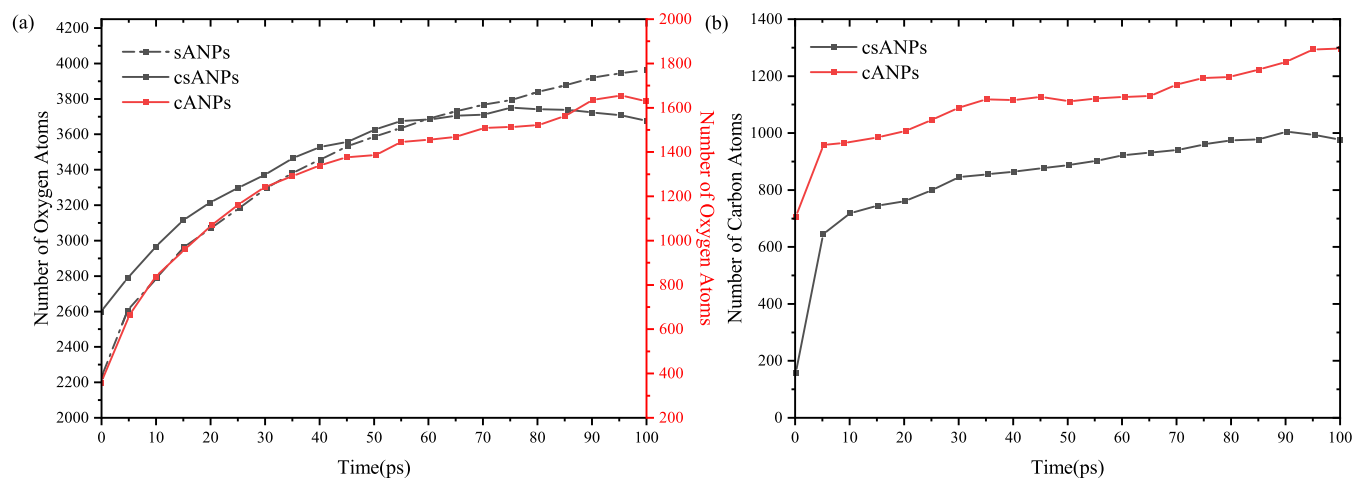
Figure 22. Curve of atomic adsorption quantity with time during combustion for (a) sANPs, csANPs, and cANPs and (b) csANPs and cANPs.

disappears at 10 ps. Figure 21(a) shows that the displacement of cAl and sO atoms tends to the same level at 10 ps, indicating that there is an almost uniform distribution of the cAl−sO mixed configuration in sANPs. In this stage, the sAl atoms are still mainly distributed in the outer oxide shell region, resulting in the movement ability of the external O_2 molecules being strong, and they are mainly adsorbed in the oxide shell region, which is difficult to penetrate the inner layer of sANPs. At this stage, due to the inward diffusion of sO, releasing more partial coordination of sAl, which makes it exhibit excellent oxidation potential. After 20 ps, sO and eO atoms begin to diffuse to the inner region of the particles, and the combustion begins to propagate inward and forms a diffusion-dominated reaction zone. Finally, sO and eO atoms propagate to the core area of particles, and all components gradually tend to be uniform. In addition, after 20 ps, although the displacement of each component in sANPs also gradually tends to be consistent, the number of external O_2 molecules continues to decline. At this time, sANPs enter the uniform combustion stage, and combustion is still ongoing. Due to the influence of the reaction temperature, the whole sANPs finally show a uniform liquid structure. As shown in Figure 21(b), for csANPs, the NC/ethanol/ether coating layer is rapidly desorbed at 3000 K, most of which diffuses to the gas phase region, and only a small part is directly involved in the surface reaction of csANPs and reacts with sAl atoms. Before 10 ps, only a few O_2 molecules can react with sAl atoms; however, the combustion process of particles will not be slowed down due to the NC molecules getting heat, and rapid pyrolysis releases heat. After 20 ps, sAl atoms begin to diffuse to the inner region and also lead to the inward diffusion of eO and organic atoms (mainly EO and DO atoms), entering the combustion propagation stage. Compared with sANPs, the solid−liquid phase structure of csANPs is more complex due to the participation of NC/ethanol/ether coating layer components. At the later stage of combustion, csANPs transformed into the Al−O−C mixed structure. In the central section configuration diagram at 60 ps, C atoms are mainly distributed in the outer layer of particles, forming a large number of Al−C bonds. It is also consistent with the reports on the formation of carbon inclusion products in Al-containing propellant combustion experiments.[38] In addition, the atomic displacement scatter plot also shows that the displacement of each component in the csANPs system does not decrease in the sANPs system at the later stage of

combustion but shows an upward trend, which further indicates that the diffusion and pyrolysis of the NC/ethanol/ ether coating layer will accelerate the multiphase reaction and promote csANPs combustion more sufficiently. As shown in Figure 21(c), the combustion process of cANPs is much faster than those of sANPs and csANPs. Since Al atoms in the oxidation shell provided by cANPs still have strong oxidation potential, the outside Al atoms react violently at the beginning of combustion, resulting in a rapid decrease in the density inside the particles, and even show a cavity phenomenon at 10 ps. In addition, the H atoms infiltrated in the coating process will generate H_2 molecules in ANPs first and then release them to the gas phase region to participate in gas phase combustion. Because cANPs do not have the oxide layer, the atom diffusivity is stronger, showing a higher combustion propagation rate and combustion efficiency. At the later combustion stage, cANPs are also transformed into an Al−O− C mixture, which is consistent with csANPs. The diffusion and pyrolysis of the NC/ethanol/ether coating layer accelerate the multiphase reaction and improve the combustion performance of cANPs.

In order to further quantitatively analyze the ANP component distribution in the combustion process, Figure 22 shows the number of O and C atoms adsorbed with time in the 2 range of the Al atom. The *Y*-axis is O atom number (a) and C atom number (b). At the early stage of combustion, the O atom adsorption rate of sANPs and cANPs is almost the same, slightly faster than csANPs. The reason is that the sO atoms in the sANP oxidation shell diffuse inward rapidly at the early stage of combustion, and the Al-rich environment is formed on the particle surface, thus adsorbing the external O_2 molecules rapidly and generating an oxidation reaction. However, as for cANPs, due to the cladding layer involved in the surface reaction, the initial O_2 adsorption rate slowed down. As for cANPs, due to the insufficient coordination number of Al atoms in the oxide layer, they also have the power to absorb external O_2 molecules rapidly. On the other hand, at the end of combustion, the oxygen adsorption rate of sANPs tends to be constant, while the adsorption rate of cANPs begins to decrease, and csANPs even begin to release some adsorbed O atoms. It is because of the further combination of Al−C bonds in the later stage, occupying the outer space of ANPs. The C atom adsorption curve also shows that csANPs and cANPs adsorb large amounts of C atoms at the early stage of
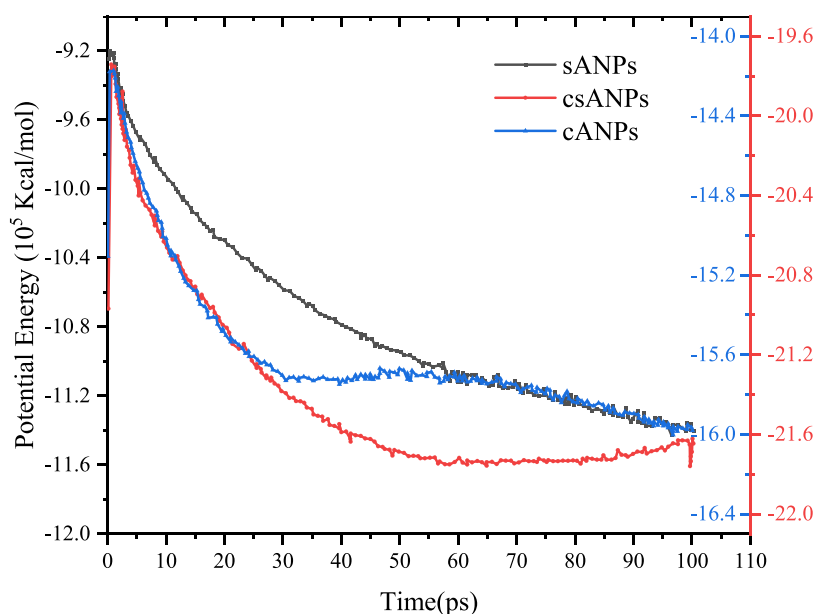
Figure 23. Curve of the potential energy change during combustion for sANPs, csANPs, and cANPs.

combustion and increase steadily at the later stage. Therefore, the C atom not only is a high-quality additional fuel source for the gas phase reaction but also participates in the solid–liquid phase combustion reaction outside ANPs directly.

Figure 23 shows the potential energy curves of sANPs, csANPs, and cANPs during combustion. Compared with sANPs, the decline rate of the potential energy curve in the early stage of the system is similar for csANPs and cANPs, higher than that for sANPs significantly. This indicates that csANPs and cANPs have a more intense combustion reaction. The slope of the potential energy curve of sANPs tends to be constant in the later stage and enters a stable and uniform combustion stage. On the other hand, the interesting thing is that the potential curves of csANPs and cANPs tend to flatten at about 55 and 30 ps, respectively, while the potential curves of cANPs begin to fall again at about 65 ps. The reason is that the existence of the NC/ethanol/ether coating layer causes the gas phase combustion in csANPs and cANPs systems, and the gas phase combustion in the cANPs system starts earlier. The breaking of the bonds of organic molecules such as NC leads to the gradual and even increase of the system's potential energy, while the large generation of gaseous molecules leads to the continuous decrease of the system's potential energy. In addition, the potential energy curves of csANPs and cANPs also reveal that the existence of the NC/ethanol/ether coating layer not only brings the occurrence of multiphase reactions but also increases the reaction time of the ANPs combustion system. It will increase the energy release time and improve the application potential in propellants.

4. CONCLUSIONS

In this study, we used MD simulations to simulate three models: passivated ANPs, NC/ethanol/ether coating-passivated ANPs, and NC/ethanol/ether coating-annealed ANPs. The analysis is carried out from the organic coating process to the ignition and combustion stages. The simulation results show that the ReaxFF-lg long-range correction reaction force field can not only capture the accurate changes of products but also accurately capture the formation and fracture of bonds in

the reaction process. During the pyrolysis of NC single-chain molecules, NC decomposes from the macromolecular chain into small molecules, while the C−O−C bond fracture in the NC molecular chain relatively lags behind. These support the research view of Wang et al. and also prove the applicability of the ReaxFF-lg long-range correction reaction force field in this study. In the preparation of the NC/ethanol/ether-coated ANPs model, we find that NC/ethanol/ether solution forms a dense coating layer on the surface of annealed ANPs and passivated ANPs through the combined action of physical and chemical adsorption. The inner side of the coating layer is a chemical adsorption layer composed of surface Al atoms and coating solution atoms. The outer side of the coating layer is a physical coating layer composed of organic molecules and residues under the action of the Coulomb force and van der Waals force. In the ignition and combustion simulation of the three models, we find that at low temperatures, the coating layer blocks the contact between the active Al core atoms and the external O_2 molecules and increases the O_2 molecular density around ANPs through adsorption. With the increase of ignition temperature and the accumulation of NC pyrolysis energy release, the NC/ethanol/ether-coated ANPs have a higher surface temperature, which can help the active Al atoms in the aluminum core diffuse to the particle surface faster. At the same time, the desorption and diffusion of the organic coating layer expose more reaction sites, and the high-density O_2 molecules around ANPs are easier to adsorb to the surface for the reaction. Thus, NC/ethanol/ether-coated ANPs have a shorter ignition delay and a lower ignition temperature. In the combustion stage, ANPs experience surface oxidation/core melting diffusion, combustion inward propagation, and uniform combustion in three stages. After the beginning of combustion, the NC/ethanol/ether coating layer desorbs and diffuses to the gas phase region rapidly, and a small part is involved in the surface oxidation of ANPs directly. The energy released by NC pyrolysis and the gas phase reaction promotes atom diffusion in ANPs and accelerates the combustion propagation rate. In addition, the C atoms in the coating layer not only are a high-quality additional fuel source for the gas

phase reaction but also participate in the solid−liquid phase combustion reaction outside ANPs directly, increasing the combustion time and efficiency of ANPs.

■ ASSOCIATED CONTENT

Data Availability Statement

The data sets used and/or analyzed during the current study are available from the corresponding author on reasonable request.

■ AUTHOR INFORMATION

Corresponding Author

Pingan Liu − *Harbin Engineering University, Harbin 150001, China; Key Laboratory of Dual Dielectric Power Technology, Hebei Hanguang Industry Co. Ltd., Handan 432000, China;* Email: liupingan631@126.com

Authors

Yue Chu − *Harbin Engineering University, Harbin 150001, China*
Lei Wang − *Harbin Engineering University, Harbin 150001, China;* ⓘ orcid.org/0000-0003-0616-8106
Penghua Sui − *Harbin Engineering University, Harbin 150001, China*

Complete contact information is available at:
https://pubs.acs.org/10.1021/acsomega.3c03547

Author Contributions

Y.C.: writing—editing. L.W.: writing—original draft and review & editing. P.L.: conceptualization, methodology, resources, and funding acquisition. P.S.: formal analysis and software.

Notes

The authors declare no competing financial interest.

■ REFERENCES

(1) Guo, L.; Song, W.; Hu, M.; et al. Preparation and reactivity of aluminum nanopowders coated by hydroxyl-terminated polybutadiene (HTPB). *Appl. Surf. Sci.* **2008**, *254* (8), 2413−2417.

(2) Sundaram, D. S.; Puri, P.; Yang, V. Pyrophoricity of nascent and passivated aluminum particles at nano-scales. *Combust. Flame* **2013**, *160* (9), 1870−1875.

(3) Yang, J.; Gong, X.; Wang, G. Density functional theory and molecular dynamic investigations on the energetic and mechanical properties of nitrocellulose/nitroglycerin/pentaerythritol diazido dinitrate composites. *Polym. Compos.* **2017**, *38* (1), 192−198.

(4) Yan, T.; Ren, H.; Li, Y.; et al. Tailoring Structural Energetics for Enhanced Reactivity of Nano-Aluminum Particles Based Microspheres. *Adv. Eng. Mater.* **2019**, *21* (8), No. 1900176, DOI: 10.1002/adem.201900176.

(5) Jacob, R. J.; Wei, B.; Zachariah, M. R. Quantifying the enhanced combustion characteristics of electrospray assembled aluminum mesoparticles. *Combust. Flame* **2016**, *167*, 472−480.

(6) Wang, H.; Jian, G.; Yan, S.; et al. Electrospray formation of gelled nano-aluminum microspheres with superior reactivity. *ACS Appl. Mater. Interfaces* **2013**, *5* (15), 6797−6801.

(7) Alavi, S.; Thompson, D. L. Molecular Dynamics Simulations of the Melting of Aluminum Nanoparticles. *J. Phys. Chem. A* **2006**, *110*, 1518−1523.

(8) korachy, E. E.; Meddad, M.; Badawi, M.; et al. Sintering and deposition of homo- and heteronanoparticles of aluminum and nickel on aluminum (100) substrate. *Chem. Phys.* **2021**, *541*, No. 11037, DOI: 10.1016/j.chemphys.2020.111037.

(9) Liu, J.; Wang, M.; Liu, P.; et al. Molecular dynamics study of sintering of Al nanoparticles with/without organic coatings. *Comput.*

(10) Nandy, J.; Sahoo, S.; Yedla, N.; et al. Molecular dynamics simulation of coalescence kinetics and neck growth in laser additive manufacturing of aluminum alloy nanoparticles. *J. Mol. Model.* **2020**, *26* (6), No. 125, DOI: 10.1007/s00894-020-04395-4.

(11) Raut, J. S.; Bhagat, R. B.; Fichthorn, K. A. SINTERING OF ALUMINUM NANOPARTICLES: A MOLECULAR DYNAMICS STUDY. *Nanostruct. Mater.* **1998**, *10*, 837−851.

(12) Song, P.; Wen, D. Molecular dynamics simulation of the sintering of metallic nanoparticles. *J. Nanopart. Res.* **2010**, *12* (3), 823−829.

(13) Zhu, H. Sintering processes of two nanoparticles: A study by molecular dynamics simulations. *Philos. Mag. Lett.* **1996**, *73* (1), 27−33.

(14) Liu, J.; Liu, P.; Wang, M.; et al. Combustion of Al nanoparticles coated with ethanol/ether molecules by non-equilibrium molecular dynamics simulations. Materials Today. *Mater. Today Commun.* **2020**, No. 100819, DOI: 10.1016/j.mtcomm.2019.100819.

(15) Wang, J.; Li, Y.; Han, Z.; et al. Study on the preparation and combustion performance of Al-F composites prepared by a solvent/non-solvent method. *Surf. Coat. Technol.* **2022**, *440*, No. 128455, DOI: 10.1016/j.surfcoat.2022.128455.

(16) Plimpton, S. Fast Parallel Algorithms for Short-Range Molecular Dynamics. *J. Comput. Phys.* **1995**, *117*, 1−19, DOI: 10.1006/jcph.1995.1039.

(17) Humphrey, W.; Dalke, A.; Schulten, K. VMD: Visual Molecular Dynamics. *J. Mol. Graphics* **1996**, *14*, 33−38.

(18) Stukowski, A. Visualization and analysis of atomistic simulation data with OVITO−the Open Visualization Tool. *Modell. Simul. Mater. Sci. Eng.* **2010**, *18* (1), No. 05012, DOI: 10.1088/0965-0393/18/1/015012.

(19) van Duin, A. C. T.; Zou, C.; Joshi, K.et al.A Reaxff Reactive Force-field for Proton Transfer Reactions in Bulk Water and its Applications to Heterogeneous Catalysis. In *Computational Catalysis*; Royal Society of Chemsitry, 2013; Chapter 6, pp 223−243.

(20) Mei, Z.; An, Q.; Zhao, F.-Q.; et al. Reactive molecular dynamics simulation of thermal decomposition for nano-aluminized explosives. *Phys. Chem. Chem. Phys.* **2018**, *20*, 29341−29350, DOI: 10.1039/c8cp05006f.

(21) Strachan, A.; Kober, E. M.; van Duin, A. C. T.; et al. Thermal decomposition of RDX from reactive molecular dynamics. *J. Chem. Phys.* **2005**, *122* (5), No. 054502, DOI: 10.1063/1.1831277.

(22) Liu, Y.; Goddard, W. A. First-Principles-Based Dispersion Augmented Density Functional Theory: From Molecules to Crystals. *J. Phys. Chem. Lett.* **2010**, *1* (17), 2550−2555.

(23) Lemak, A. S.; Balabaev, N. K. On The Berendsen Thermostat. *Mol. Simul.* **1994**, *13* (3), 177−187.

(24) Liu, J.; Wang, M.; Liu, P. Molecular dynamical simulations of melting Al nanoparticles using a reaxff reactive force field. *Mater. Res. Express* **2018**, *5* (6), No. 065011, DOI: 10.1088/2053-1591/aac653.

(25) Evans, D. J.; Holian, B. L. The Nose−Hoover thermostat. *J. Chem. Phys.* **1985**, *83* (8), 4069−4074.

(26) Liu, P.; Liu, J.; Wang, M. Ignition and combustion of nano-sized aluminum particles: A reactive molecular dynamics study. *Combust. Flame* **2019**, *201*, 276−289.

(27) Di Tommaso, S.; Rotureau, P.; Crescenzi, O.; et al. Oxidation mechanism of diethyl ether: a complex process for a simple molecule. *Phys. Chem. Chem. Phys.* **2011**, *13* (32), 14636−14645.

(28) Mei, Z.; An, Q.; Zhao, F. Q.; et al. Reactive molecular dynamics simulation of thermal decomposition for nano-aluminized explosives. *Phys. Chem. Chem. Phys.* **2018**, *20* (46), 29341−29350.

(29) Gao, Y.; Zhu, W.; Wang, T.; Yilmaz, D. E.; Van Duin, A. C. C/H/O/F/Al Reaxff force field development and application to study the condensed-phase poly(vinylidene fluoride) and reaction mechanisms with aluminum. *J. Phys. Chem. C* **2022**, *126* (27), 11058−11074.

(30) Mao, Q.; Rajabpour, S.; Kowalik, M.; van Duin, A. C. Predicting cost-effective carbon fiber precursors: Unraveling the

Mater. Sci. **2021**, *190*, No. 110265, DOI: 10.1016/j.commatsci.2020.110265.

functionalities of oxygen and nitrogen-containing groups during carbonization from ReaxFF simulations. *Carbon* **2020**, *159*, 25−36.

(31) Hong, S.; van Duin, A. C. Molecular dynamics simulations of the oxidation of aluminum nanoparticles using the ReaxFF reactive force field. *J. Phys. Chem. C* **2015**, *119* (31), 17876−17886.

(32) Jutier, J.-J.; Harrison, Y.; Premont, S.; et al. A Nonisothermal Fourier Transform Infrared Degradation Study of Nitrocelldoses Derived from Wood and Cotton. *J. Appl. Polym. Sci.* **1987**, *33*, 1359−1375, DOI: 10.1002/app.1987.070330424.

(33) Martínez, L.; Andrade, R.; Birgin, E. G.; et al. PACKMOL: a package for building initial configurations for molecular dynamics simulations. *J. Comput. Chem.* **2009**, *30* (13), 2157−2164.

(34) Sundaram, D. S.; Puri, P.; Yang, V. A general theory of ignition and combustion of nano- and micron-sized aluminum particles. *Combust. Flame* **2016**, *169*, 94−109.

(35) Chakraborty, P.; Zachariah, M. R. Do nanoenergetic particles remain nano-sized during combustion? *Combust. Flame* **2014**, *161* (5), 1408−1416.

(36) Trunov, M. A.; Schoenitz, M.; Dreizin, E. L. Effect of polymorphic phase transformations in alumina layer on ignition of aluminium particles. *Combust. Theory Modell.* **2006**, *10* (4), 603−623, DOI: 10.1080/13647830600578506.

(37) Doi, R.; Nakagaki, M.; Kuwahara, T. In *Surface Temperature of Agglomerated Aluminum Particle in the Reaction Zone of AP/HTPB Composite Propellants*, 51st AIAA/SAE/ASEE Joint Propulsion Conference; AIAA, 2015.

(38) Ao, W.; Liu, P.; Yang, W. Agglomerates, smoke oxide particles, and carbon inclusions in condensed combustion products of an aluminized GAP-based propellant. *Acta Astronaut.* **2016**, *129*, 147−153.